Design of Dual-Band Uncooled Infrared Microbolometer

Qi Cheng, *Student Member, IEEE*, Suzanne Paradis, Truc Bui, and Mahmoud Almasri, *Member, IEEE*

Abstract—This paper describes the design and modeling of a smart uncooled infrared detector with wavelength selectivity in the long-wavelength infrared (LWIR) band. The objective is to enhance the probability of detecting and identifying objects in a scene. This design takes advantage of the smart properties of vanadium dioxide (VO_2): it can switch reversibly from an IR-transparent to an IR-opaque thin film when properly triggered. This optical behavior is exploited here as a smart mirror that can modify the depth of the resonant cavity between the suspended thermistor material and a patterned mirror on the substrate, thereby altering wavelength sensitivity. The thermistor material used in the simulation is vanadium oxide (VO_X). The simulation results show that, when VO_2 is used in the metallic phase, it reflects IR radiation back to the suspended VO_X and enhances IR absorption in the 9.4–10.8-μm band. When the film is switched to the semiconductor phase, it admits most IR radiation, which is then reflected back to the suspended VO_X by a patterned gold thin film under an SiO_2 spacer layer. The spacer layer is used to increase the resonant cavity depth underneath the microbolometer pixel. Thus, the peak absorption value is shifted to 8–9.4 μm, creating the second spectral band. The detector is designed with a relatively low thermal conductance of 1.71×10^{-7} W/K to maximize responsivity (R_v) to values as high as 1.27×10^5 W/K and detectivity (D^*) to as high as 1.62×10^9 cm·Hz$^{1/2}$/W, both at 60 Hz. The corresponding thermal time constant is equal to 2.45 ms. Hence, these detectors could be used for 60-Hz frame rate applications. The extrapolated noise equivalent temperature difference is 14 and 16 mK for the 8–9.4- and 9.4–10.8-μm bands, respectively. The calculated absorption coefficients in the two spectral bands were 59% and 65%, respectively.

Index Terms—Dual-band infrared (IR) detector, microbolometer, vanadium oxide (VOx).

I. INTRODUCTION

INFRARED (IR) imaging cameras detect variations in heat and create an electronic image of everything in view. The images generated by typical single-band cameras show the surface temperature variations of objects in a scene in black-hot mode. The capability of an IR detector to switch wavelength sensitivity between two bands enhances the probability of detecting and identifying objects in a scene. Commercial multiband IR cameras are currently available. They typically use two separate focal plane arrays (FPAs) and electronics for each spectral band or a single FPA and an optical element that selects the appropriate spectral band (filter wheel or spectral dispersion techniques) [1], [2]. The use of separate FPAs has several drawbacks, including significant added complexity and cost and the challenge of alignment between the FPAs. These approaches are effective for certain applications, but they have proven to be bulky and costly [3]. Cooled multiband FPAs are based on mercury cadmium telluride (MCT), quantum-well IR photodetectors using III-V materials, and quantum-dot IR photodetectors [4]–[7]. These detectors offer many advantages such as high sensitivity and very high speed, but require expensive and heavy cryogenic equipment to operate. These are used for military applications where ultrahigh sensitivity and speed are required. For a wide range of applications that do not require ultrahigh sensitivity, however, the high cost of cooling becomes a problem. The development of an uncooled dual-band detector would retain the advantages of uncooled detectors over cooled detectors, which are: much lower fabrication cost (no exotic and difficult to produce semiconductor materials), reduced weight, size, and energy consumption (no bulky and noisy cooling system required). The commercial and defense sectors would both benefit from uncooled dual-band cameras: highway safety, medical diagnostics and surgery, surveillance, law enforcement, and security. Dual-band cameras also offer a possible solution for real-time detection and identification of carefully concealed targets even in cluttered environments (environments with unwanted parasite signals). Having two bands instead of one will ease clutter rejection and therefore plays a significant role in discriminating the actual temperature and unique signature of objects in the scene [8]–[16]. No attempt was made in this study to tune from long-wavelength IR (LWIR) to mid-wavlength IR (MWIR). The reason is that the sensitivity attainable in the MWIR with the current state-of-the-art uncooled microbolometer does not meet the typical sensitivity requirements of surveillance systems. However, an IR camera offering wavelength selectivity in the LWIR band has shown promise in the detection of such difficult targets as recently buried mines [17]. Recently, monolithic detectors offering dual-band tunability have been investigated: wavelength-selective IR microbolometers using planar multimode detectors [18] and two-color thermal detectors [19] have been designed, and adaptive microbolometers have been designed, fabricated, and characterized [20]. These detectors were designed to operate in the LWIR band. In the first two designs, the cavity was tuned by using movable micromirrors underneath the microbolometer pixel, while in the third design the cavity was tuned by moving the microbolometer pixel via

electrostatic actuation. The first approach has not been realized, while the second approach has achieved low responsivity and detectivity [20]. These designs are relatively complicated since they require movable components.

VO$_2$ belongs to a family of materials (termed chromogenic) which are capable of reversibly modifying their optical and electrical properties upon specific stimulation such as temperature, pressure or electrical field. The phase transition of VO$_2$, which is triggered at 68 °C, is responsible for its optical and electrical modulation. At room temperature, the film behaves as a semiconductor material with an energy bandgap of ∼0.7 eV. When the temperature is increased to 68 °C, the energy bandgap vanishes, the lattice becomes tetragonal, and the film behaves as a metal. The electrical resistivity of the film can be varied by three to four orders of magnitude, and the film can be changed from IR-transparent in the semiconducting phase to IR-reflective in the metallic phase [21]–[27]. These features have prompted many groups to use VO$_2$ at the phase transition for electrooptical switches [26], [27]. We have used the VO$_2$ stochiometry to design the smart mirror because no other oxide of vanadium has the stochiometry needed to engender the desired chromogenic behavior. VO$_X$ (nonstochiometric film) in the semiconducting phase is selected as an IR-sensitive material because of its high-temperature coefficient of resistance, low $1/f$ noise, and low resistance, which is compatible with readout electronics. Several other materials can be used for IR detection, including amorphous silicon (a: Si) [28], yttrium barium copper oxide (YBaCuO) [29], silicon germanium (SiGe) [30], silicon germanium oxide (SiGeO) [31], [32], and metals [33]. In this paper, a dual-band microbolometer model is presented. It can be tuned to two spectral bands (with some overlap) without using a movable structure, and hence the same microfabrication procedures developed for single-band microbolometers can be used to fabricate the proposed device.

II. BACKGROUND AND THEORY

A microbolometer is a thermal sensor whose resistance changes with temperature, associated with the absorption of IR radiation. Its performance is characterized by several figures of merit such as responsivity (R_v), temperature coefficient of resistance (TCR), detectivity (D^*), and noise equivalent temperature difference (NETD) [34]. Responsivity is the output voltage divided by the input radiant power falling on the detector. It is given by

$$R_v = \frac{I_b R \eta \beta}{G \left(1 + \omega^2 \tau_{\text{th}}^2\right)^{1/2}} \quad (1)$$

where I_b is the bias current (A), R is the bolometer electrical resistance (Ω), η is the fraction of the incident radiation absorbed, G is the total thermal conductance to the substrate (W/K), ω is the radiation modulation frequency, τ_{th} is the thermal response time, and β is used to quantify the temperature dependence of resistance to measure the heating effect of the absorbed IR radiation and is given by

$$\beta = \frac{1}{R} \frac{dR}{dT}. \quad (2)$$

The detectivity $D*$ is a figure of merit (FOM) that measures the signal-to-noise ratio (SNR) and normalizes the performance of the detector with respect to the detector size and is given as

$$D^* = \frac{R_v \sqrt{A \Delta f}}{\Delta V_n} \quad (2)$$

where Δf is the amplifier frequency bandwidth (Hz), A is the detector area (cm^2), and ΔV_n is the total noise voltage of the system (V). Hence, for good performance, a microbolometer must have large values of β, R_V, and $D*$, [35].

The NETD is a camera FOM given by

$$\text{NETD} = \frac{4F^2}{\tau_0 A^{1/2} D^* (\Delta M / \Delta T)_{\lambda_1 - \lambda_2}} \quad (4)$$

where F is the focal ratio of the optics, τ_0 is the transmittance of the optics, and $(\Delta M / \Delta T)_{\lambda_1 - \lambda_2}$ is the change in optical power emitted with respect to temperature per unit area radiated by a blackbody at temperature T measured within the spectral band from λ_1 to λ_2. Note that total noise must be minimized and the responsivity must be maximized to achieve the best sensitivity. High sensitivity can be achieved by maximizing R_V, and D^* and TCR. The thermal time constant τ_{th} was calculated from the ratio of the device's thermal mass to its thermal conductance, C/G_{th}. The thermal mass of the microbolometer is given by

$$C = \sum_n W_n L_n t_n c_n + \frac{1}{3} \sum_m W_m L_m t_m c_m \quad (5)$$

where W_n, L_n, and t_n correspond to width, length, thickness, and specific heat of each thin film layer, and W_m, L_m, t_m, and c_m correspond to width, length, thickness, and specific heat of each layer of the electrode arms. The total thermal conductance of the microbolometer is given by

$$G_{\text{tot}} = \sum_m \frac{K_m W_m t_m}{L_m} \quad (6)$$

where K_m is the thermal conductivity of each component, and W_m, L_m, and t_m correspond to width, length, and thickness of each component. The thermal time constant τ_{th} was calculated from the ratio of the device's thermal mass to its thermal conductance, C/G_{th}.

The microbolometer presented here consists of an IR-sensitive element deposited on top of a microbridge and suspended above the substrate by support arms. The gap between the IR-sensitive element and the IR-reflective mirror patterned on the substrate plays an important role in the absorption of IR radiation for the suspended microbolometer since it is wavelength-dependent. With the appropriate design, this gap behaves as a Fabry–Perot resonant cavity which maximizes IR absorption and hence maximizes responsivity and detectivity. The resonant cavity can be created between the incoming and reflected waves if the cavity depth is tuned accordingly:

$$d_n = [(2n - 1) - (\varphi_1 - \varphi_2)] \frac{\lambda}{4} \quad (7)$$

where d_n is the air gap depth, n is an integer, λ is the wavelength, and φ_1 and φ_2 are the phase differences between the incoming and reflected light [36]. In operation, the microbolometer requires either current or voltage biasing. The Infrared camera
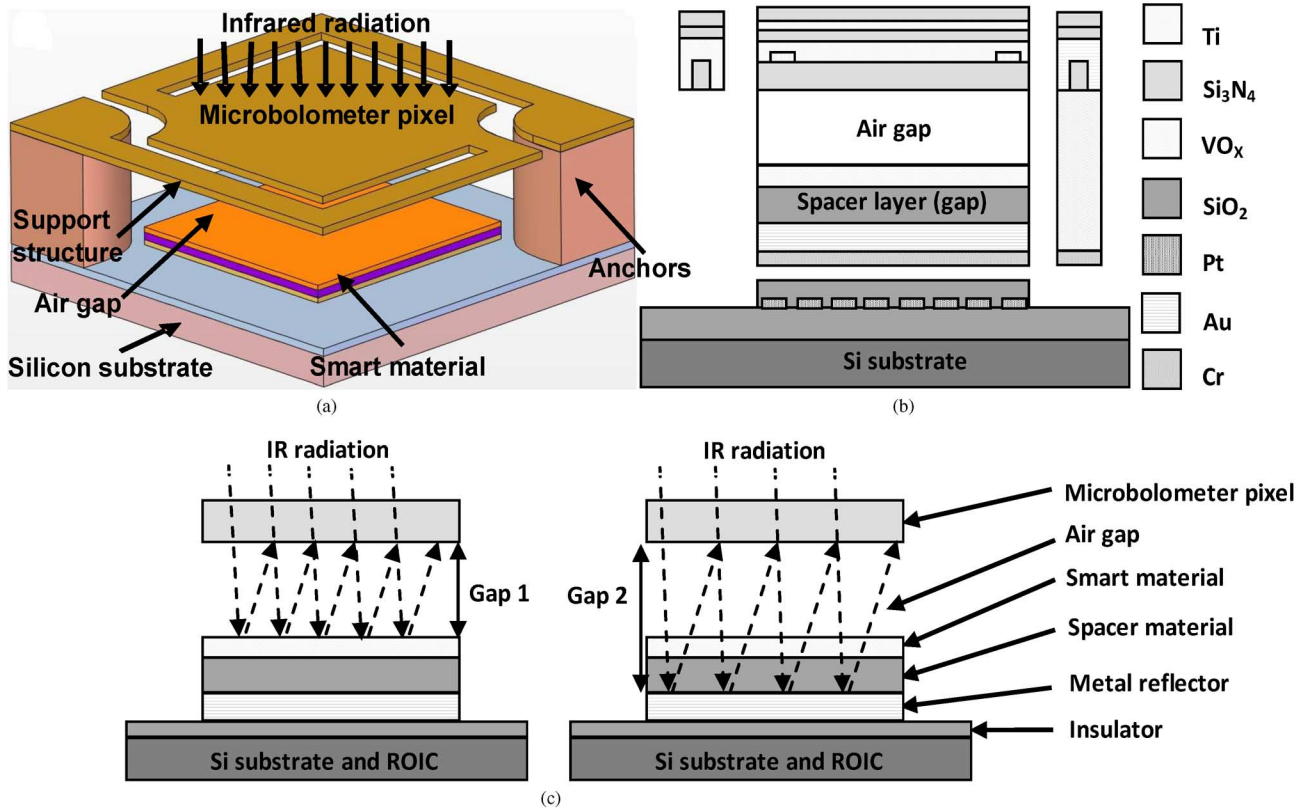
Fig. 1. Schematics show the dual-band microbolometer in (a) 3-D view, (b) side view, and (c) operational view. IR radiation is reflected by the smart material when it is used in the metallic phase [(c), left], and is reflected by the gold layer when the smart material is used in the semiconducting phase.

that are based on microbolometer focal plane array do not require chopper for operation. However, for modeling and testing the individual devices, a chopper is used in order to enable the calculation of the cut off frequency and the video frame rate.

III. MICROBOLOMETER DESIGN

The uncooled microbolometer design takes advantage of the smart properties of VO_2: it can switch reversibly from an IR-transparent to an opaque thin film when properly triggered. This optical behavior is exploited here as a smart mirror that can modify the Fabry–Perot resonant cavity depth between the suspended thermistor material VO_X) and a mirror patterned on the substrate, thereby altering wavelength sensitivity and creating a dual-band microbolometer. A schematic of the dual-band microbolometer along with the structural view and operational view are shown in Fig. 1. The fixed reflective mirror is switching between the smart material (VO_2) and Au layer. In the first case, the VO_2 is used in the metallic phase by heating the detector to 68 °C. Thus, the IR radiation is reflected back to the suspended VO_X enhancing the IR absorption in the first spectral band (9.4–10.8 μm). In the second case, VO_2 is switched to the semiconducting phase by cooling the detector to room temperature. Thus, most of the IR radiation is transmitted through the transparent VO_2 layer and through a SiO_2 layer used as a spacer material, and then reflected by the gold (Au) thin film mirror layer, which is patterned underneath the SiO_2 spacer layer on the substrate. Thus, the gap underneath the microbolometer pixel, which initially contained only vacuum,

is increased by the thicknesses of the SiO_2 and VO_2 transparent materials. Therefore, the IR absorption is shifted to a second spectral band (8–9.4 μm). The resonant cavity depths are optimized to maximize IR absorption, thereby increasing the responsivity and detectivity of the microbolometer in the 8–9.4- and 9.4–10.8-μm spectral bands. The two-band design enhances the probability of detecting and identifying objects in a scene. These two windows were chosen for demonstration of concept: they split the 8–12 μm LWIR band roughly in two.

Thin-film Wizard software (Film Wizard) developed by Scientific Computing International (SCI-Soft) is used to determine the absorption of the microbolometer for the case of normal incidence of the radiation using the refractive index $((n(\lambda))$ and absorption coefficient $(k(\lambda))$ of the various layers, which include the VO_x IR-sensitive layer, Si_3N_4 bridge, Ti absorber, Si_3N_4 passivation layers, VO_2 reflective/transparent layer, SiO_2 spacer layer, Au reflective mirror, chromium (Cr) adhesive layer, SiO_2 insulating layer and silicon substrate. The thin film layer thicknesses and the gap depths were adjusted until the maximum absorption in the specified wavelength windows is determined. The result was absorption with an average value of 65% and 59% for cavity depths of 3.9 and 4.63 μm, respectively. In the first case, the absorption was maximized for the 9.4–10.8-μm band, while in the second case the absorption was maximized for the 8–9.4-μm band. The absorption was plotted as a function of wavelength for both cavity depths, as shown in Fig. 2. In addition, the difference in absorption value between 8–9.4- and 9.4–10.8-μm bands for metallic and semiconductor phases respectively were 40.6%, and 32%. This difference in absorption
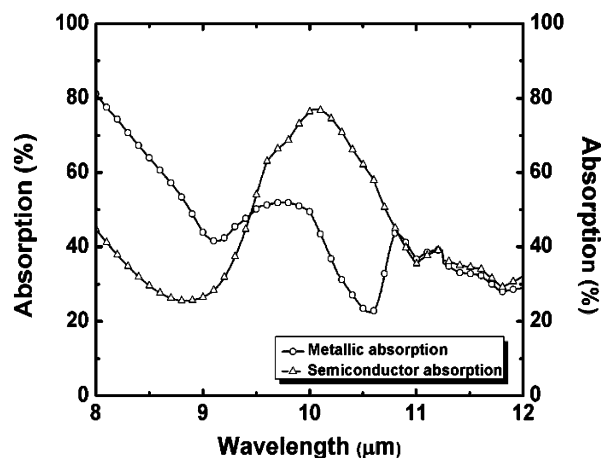
Fig. 2. Calculated optical absorption for the metallic phase (9.4–10.8 μm) and semiconducting phase (8–9.4 μm) of VO_2 are plotted as a function of wavelength for cavity depths of 3.9 and 4.63 μm, respectively.
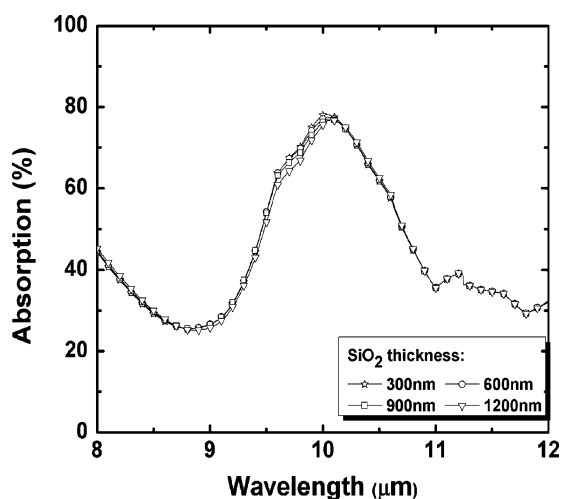

Fig. 3. Calculated optical absorption are plotted as a function of wavelength. VO_2 is used as a reflector. The air gap is fixed at 3.9 μm while the SiO_2 spacer layer is variable, and all other films are of fixed thickness.
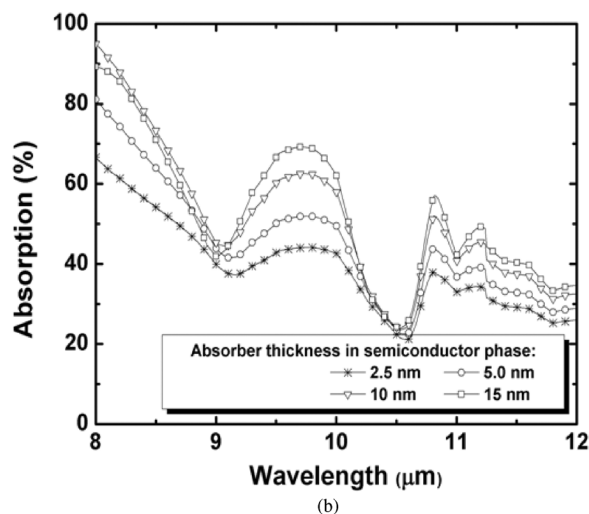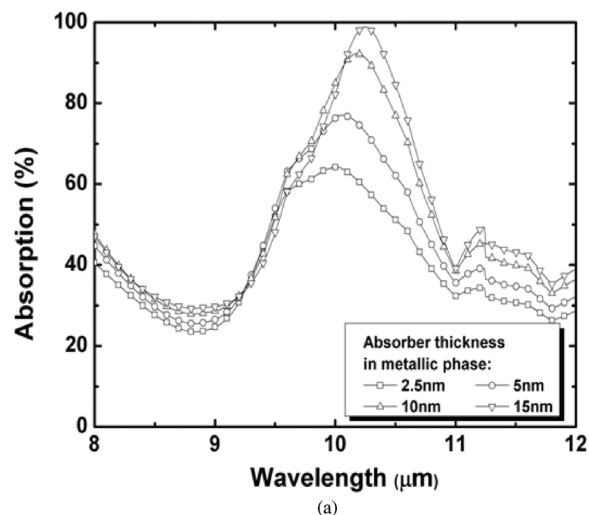

(a)

(b)

Fig. 4. Microbolometer optical absorption is plotted versus wavelength. The Ti absorber thickness is variable while all other films are of fixed thickness (see Table I). VO_2 is used in (a) metallic phase and (b) semiconducting phase.

can be seen as the contrast between the two modes. The $n(\lambda)$ and $k(\lambda)$ of the VO_2 and Si_3N_4 thin-film layers were found in the literature [37] for the former, and in FilmStar Optical Thin Film Software for the latter. When VO_2 with a thickness of 130 nm is used in the metallic phase, the IR radiation was reflected back to the suspended VO_X IR-sensitive layer. The absorption results were not affected by changing the SiO_2 spacer layer thickness. This suggests that the selected VO_2 thickness is satisfactory for reflecting most of the IR radiation (Fig. 3). It is important to note that the electrical, mechanical, thermal, and optical properties are optimized simultaneously in order to design a high-performance microbolometer. The thickness of VO_2 was fixed at 130–150 nm in the model. This thickness was optimized by the coauthor's laboratory [21], [22].

The microbolometer is designed with a pixel size of 25×25 μm^2, enabling the fabrication of mega-pixel format arrays. Each microbolometer consists of an Si_3N_4 bridge with a thickness of 350 nm suspended above a silicon substrate. Si_3N_4 is used because of its excellent thermal properties, processing characteristics and high IR absorption. Encapsulated

in the center of the Si_3N_4 bridge is a layer of VO_X IR-sensitive material and thin Ti absorber with thicknesses of 150 and 10 nm, respectively. A layer of Si_3N_4 with a thickness 50 nm was used to prevent electrical contact between the VO_X and the Ti absorber. The VO_X thickness is optimized experimentally to achieve high TCR, low resistivity, and low noise properties. The Ti was chosen as an absorber with this thickness since it maximizes the absorption difference between metallic and semiconducting phases in each spectral band. Thus, it increases IR absorption in the 9.4–10.8-μm band and decreases it in the 8–9.4-μm band when the underlying VO_2 is used in the metallic phase. When the VO_2 is switched to the semiconducting phase, IR absorption is decreased in the 9.4–10.8-μm band and increased in the 8–9.4-μm band. The effects of the Ti absorber thickness on absorption are shown in Fig. 4. Several other metals such as nickel–chromium (Ni-Cr) and platinum (Pt) could be used as an absorber. Atop the Ti absorber, a third layer of Si_3N_4 is deposited and patterned with a thickness of 50 nm in order to passivate and, hence, protect it from oxidation during the removal of the polyimide sacrificial layer using oxygen plasma to release the microbolometer. The

TABLE I
MICROBOLOMETER PIXEL AND SUPPORT ARM LAYERS THICKNESSES THAT
ARE USED IN THE MODEL. THE PIXEL, SUPPORT ARM, AND AU CONTACTS
SIZES ARE $25 \times 25\ \mu M^2$, $54 \times 4\ \mu M^2$, AND $23 \times 4\ \mu M^2$, RESPECTIVELY

Layers	Pixel Thickness (nm)	Arm thickness (nm)
Ti absorber	10	-
VO_X (Semicond ph.)	150	-
Si_3N_4	400	350
Au contact	100	-
Ti electrodes	100	100
Air gap	3.9 μm	-
VO_2 Mirror/ transparent	130	-
SiO_2 spacer layer	600	-
Au mirror	200	-
Chromium adhesion layer	150	-
SiO_2 insulating layer	200	-
Si substrate	Thick	-

TABLE II
SPECIFIC HEAT AND THERMAL CONDUCTIVITY USED IN THE MODEL AND THE
CALCULATED THERMAL MASS AND THERMAL CONDUCTANCE OF EACH LAYER

Layers	Heat capacity (Joule/K.cm^3)	Thermal Conductivity (W/cm.K)	Thermal Conductance $G_{th}(10^7 \times W/K)$	Thermal Mass $C_{th}(10^{10} \times J/K)$
Ti	2.266	0.217	-	0.14
Si_3N_4	5.413×10^{-4}	0.003	0.0889	1.35
VO_X	2.316	0.307	-	1.88
Au	2.482	3.15	-	0.17
Ti	-	0.217	1.62	-

bridge arms are made of Si_3N_4 and Ti layers with an area of $54 \times 4\ \mu m^2$. The arms serve as support structures, conductive legs, and thermal isolation legs. Au was used as the contact (area $23 \times 4\ \mu m^2$) because it makes excellent contact with the VO_X IR-sensitive layer resulting in linear behavior. We selected Ti as the electrode material because it has a much lower thermal conductivity than Au, thus providing better thermal isolation. Vacuum cavities with depths of 3.9 and 4.63 μm are used to create the wavelength resonant cavities at two separate windows. This difference in absorption can be seen as the contrast between the two modes. The first cavity is between the suspended VO_X and the underlying VO_2 in the metallic phase. The vacuum cavity also provides thermal isolation from the substrate. The second cavity is between the suspended VO_X and the underlying Au mirror. This cavity consists of vacuum and SiO_2 spacer material and VO_X layer. Finally, a silicon substrate with a resistivity of 10 $\Omega \cdot cm$ is used. A complete list of the calculated film thicknesses and their electrical and thermal properties are shown in Table I. The thermal mass and thermal conductance were calculated for the microbolometer with pixel, support arm, and Au contact areas of $25 \times 25\ \mu m^2$, $54 \times 4\ \mu m^2$, and $23 \times 4\ \mu m^2$ as shown in Table II.

The pixel was designed with low thermal mass (4.48×10^{-10} J/K) and the supporting arms with relatively low thermal conductance (1.71×10^{-7} W/K), to reduce the thermal time constant (2.6 ms) and maximize responsivity and detectivity. The thermal conductance through the electrode arms is made as small as possible to meet response time requirements. We aimed for a low thermal time constant for high-speed camera applications. The thermal mass of the microbolometer was calculated from the specific heat capacity and volume of each layer forming the microbridge and 1/3 of each Au/Si_3N_4 electrode arm. The thermal conductance was estimated from the calculated thickness, width, and length of the electrode arms that were obtained from the electromechanical model results. It was also obtained from the thermal simulation. Since the thermal conductance of the two components making up the electrode arms were in parallel, the total thermal conductance was determined by summing the thermal conductance of the different layers. Thermal conduction occurs mainly through the electrode arms and the surrounding air. Therefore, the electrode arms were carefully designed to reduce the thermal conductance path and to meet the thermal time response requirements. The pixel array will be packaged in a vacuum in order to thermally isolate the IR-sensitive element from its surroundings to reduce the rate of heat loss, thereby increasing the sensitivity of the detector.

IV. STRUCTURAL AND THERMAL SIMULATION

Finite-element analysis using CoventorWare was employed to provide an accurate prediction of the microbolometer performance. The simulations were performed using published material properties of all thin film layers. The resulting stress distribution (Von Mises) of the electrode arms and the pixel due to the internal forces acting on the microbolometer, which includes the axial force, shear, moment, and torque, were calculated and plotted in Fig. 5 for the case when the heater is in the off-state. In general, the result shows that the microbolometer with a $25 \times 25\ \mu m^2$ pixel and $54 \times 4\ \mu m^2$ support arms has flat surfaces and low stress distribution. The deflection of the electrode arms and the pixel was negligible, at $2.77 \times 10^{-5}\ \mu$ m. A detailed thermal simulation of the dual-band microbolometer was performed using CoventorWare. The simulation was performed by assuming an input heat power of 3×10^7 W/m^3, which corresponds to a constant power of 0.264 μW absorbed by the VO_X IR-sensitive layer. This power increases the microbolometer temperature from a reference temperature of 300 K (room temperature) to 301.53 K on the pixel, which is reached in steady state simulation. The applied input power and the corresponding temperature rise of the microbolometer are used to calculate the thermal conductance as 1.72×10^{-7} W/K. The temperature gradient across the microbolometer was simulated in vacuum condition with respect to the reference temperature (300 K) and shown in Fig. 6(a). The heat flux distribution is shown in Fig. 6(b), with the heat flux highest at the support arm. The simulated and calculated thermal conductance were essentially the same, which confirms the accuracy of the model. The stress distribution and the temperature gradient across the microbolometer for the case when the heater is in the on-state is expected to be similar to the off-state. Voltage application on the dedicated microheater which is located underneath the VO_2 induces heating via Joule
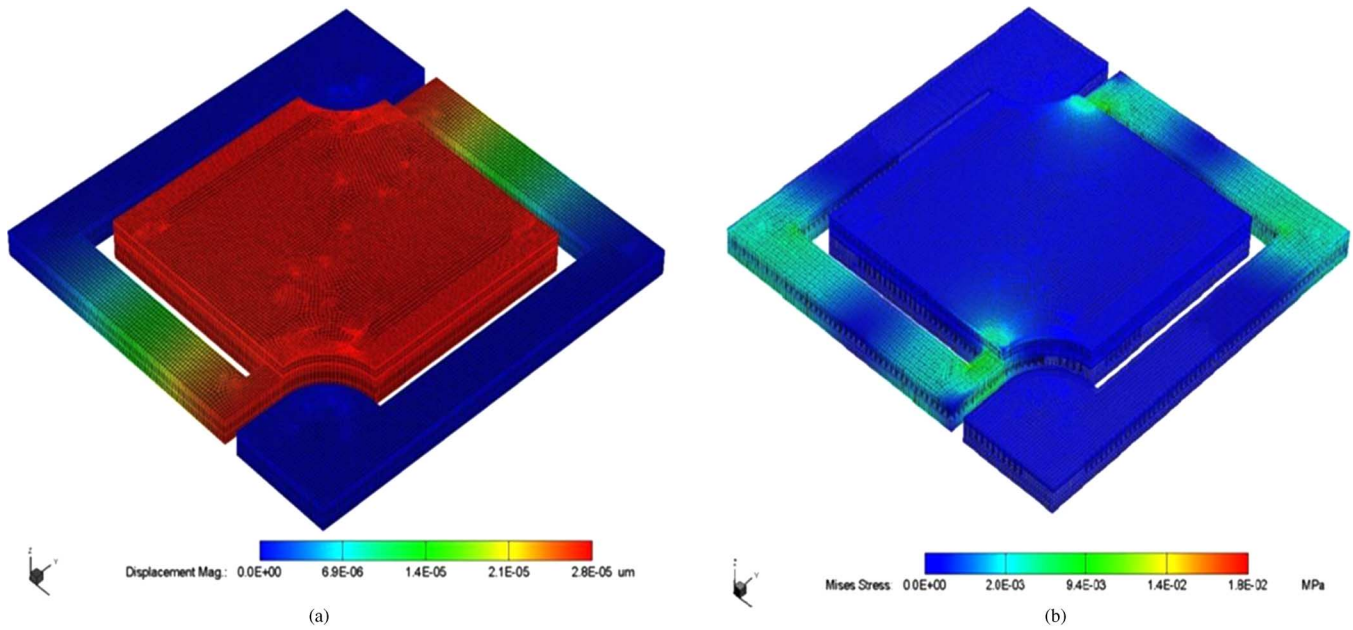
Fig. 5. Plots show (a) an optimized microbolometer structure, with pixel and support arm size of 25×25 μm^2 and 54×4 μm^2, with relatively little deflection. The largest deflection occurs at the corners of the square pixel with a value of 2.77×10^{-5} μm. (b) Von Mises stress distribution of the microbolometer with flat surface. The greatest stress -1.8×10^{-2} MPa—occurs at the joints between support arms and fixed anchors. The simulation was performed using Coventor finite-element tool.
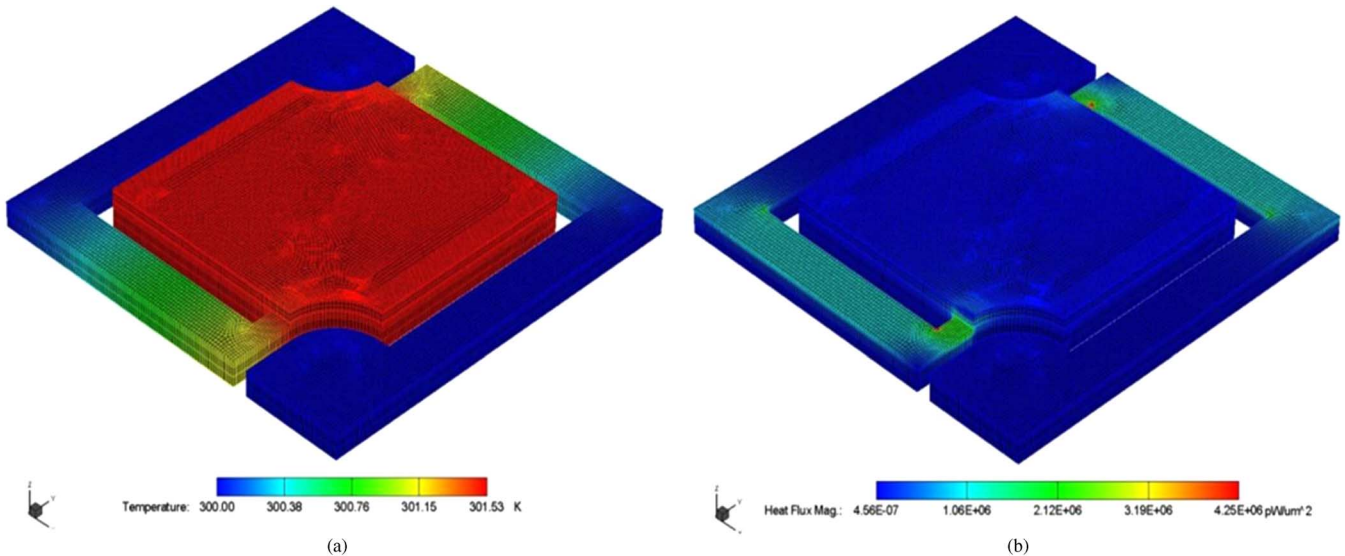

Fig. 6. (a) Temperature gradient across the microbolometer structure with pixel and support arm size of 25×25 μm^2 and 54×4 μm^2. The highest temperature (301.53 K) occurs in the pixel in steady-state simulation. (b) Heat flux distribution across the microbolometer structure.

effect. The response time for the transition by Joule effect is a function of the quality of the contact and the surface area to be heated. The response time and down time are expected to be in microseconds range. However, this needs to be confirmed by experimentally. On the other hand, the VO_x switches between the two metallic and semiconductor phases at a rate double the camera frame rate (60 Hz). Therefore, the resonant cavity depth (gap) changes between two positions and hence provides a response to two spectral windows. In other words, the total thermal response time for both spectral windows is 2.6 ms. This response time will be divided equally between the two spectral window, each 1.3 ms. This time is much higher than the microheater's response time and down time.

The dual-band microbolometer can be realized by employing a series of photolithography, surface micromachining and polyimide sacrificial layer processes in the following sequence [see Fig. 1(b)].

1) The wafer is thermally oxidized to grow a thick SiO_2 layer for insulation.
2) Pt layer is deposited and patterned to form the heater.
3) A layer of oxide is deposited using PECVD for insulation.
4) A thin layer of chromium (Cr) and a thin layer of gold (Au) is sputter-deposited and patterned to form the reflective mirror, trace line and bonding pads.
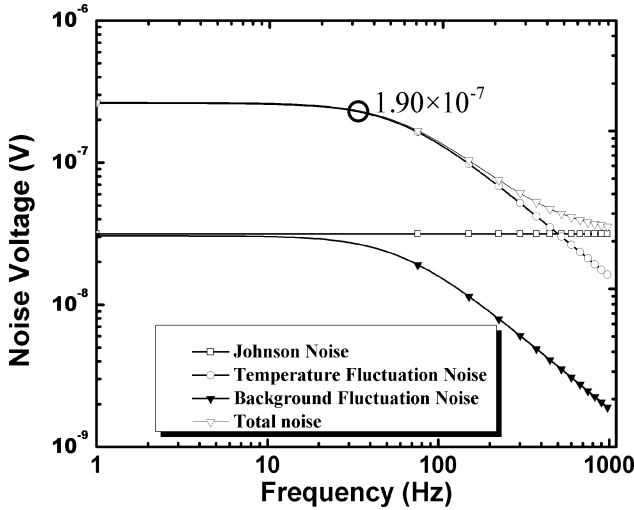5) A thick layer SiO_2 spacer material is deposited and patterned.

Fig. 7. Johnson noise, temperature fluctuation noise, background fluctuation noise, and total noise were calculated as a function of chopper frequency.

6) A layer of VO_2 is deposited and patterned. This layer will be used as a reflecting mirror when operated in the metallic phase, and will transmit IR radiation through it when switched to the semiconducting phase.

7) A polyimide sacrificial layer is spin-coated, patterned the gap and a mold for fabricating the anchors.

8) A photoresist layer is spin-coated and patterned at locations corresponding to the microbolometer anchors.

9) Ti is then sputter-deposited and patterned using a lift-off technique to create the microbolometer anchors.

10) The photoresist is removed with acetone.

11) A thick layer of Si_3N_4 is deposited and patterned to form the bridge structure.

12) The VO_X IR-sensitive material is sputter-deposited and patterned.

13) Au is deposited and patterned to create the support arms and electrode contacts.

14) A thin layer of Si_3N_4 is deposited and patterned for insulation, followed by sputtering of a thin Ti absorber.

15) The absorber is then patterned.

16) A third layer of Si_3N_4 is deposited and pattern to protect the absorber.

17) All Si_3N_4 layers are patterned and dry etched to expose the polyimide to oxygen ashing in the final step.

18) The polyimide sacrificial layers are removed by oxygen plasma ashing.

V. MICROBOLOMETER PERFORMANCE

Prior to calculating performance, the microbolometer is assumed to have a TCR and a resistance of 100 K·Ω and 2.7%/K, respectively, based on published data in the literature. It will be dc-biased with a bias current of 25 μA. Performance is calculated for the microbolometer with a support arm size of 54×4 μm^2. Initially, the total noise, which includes Johnson noise, temperature fluctuation noise, and background fluctuation noise, was calculated as a function of chopper frequency and plotted in Fig. 7. It is important to note that uncooled thermal cameras since it will allow the detector to reach the background
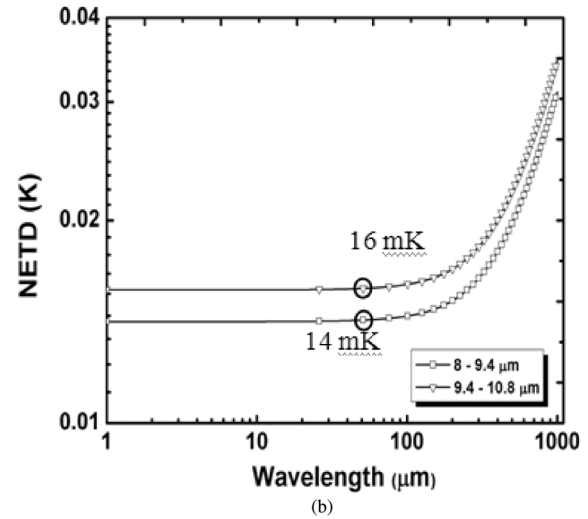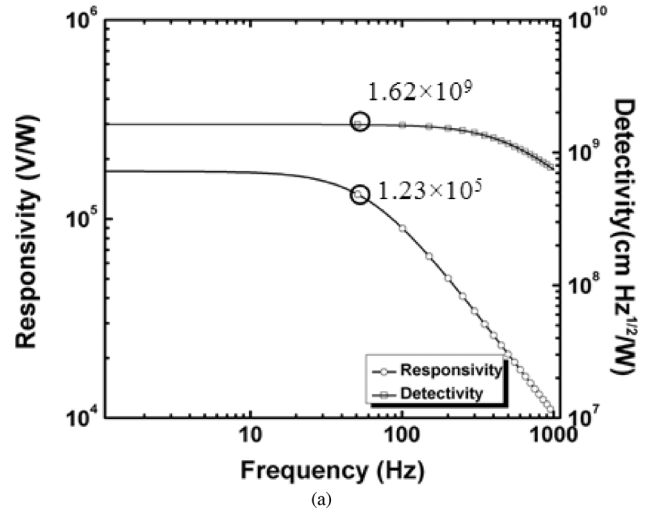

Fig. 8. (a) Responsivity and detectivity and (b) NETD as a function of chopper frequency. The $D*$ and R_v values for both spectral bands are almost same.

limited noise performance and further improve NETD. The $1/f$ noise was not accounted for in the calculation of the total noise because the detector will be biased in the Johnson-noise-level region and the $1/f$ noise depends on many process technology factors related to the microbolometer fabrication. In addition, VO_x has low $1/f$ noise. Therefore, the $1/f$ noise does not affect the capabilities of the proposed design. The voltage responsivity and detectivity were calculated for the two spectral bands and plotted versus chopper frequency in Fig. 8. The highest achieved values at 60-Hz frame rate were 1.23×10^5 V/W and the reduction of noise is crucial to the next generation of 1.62×10^9 cm sqrt(Hz/W). The responsivity was maximized by enhancing the absorption to 61% and 63% for the 8–9.4- and 9.4–10.8-μm bands, and by achieving relatively low thermal mass (J/K) and low thermal conductance (W/K) in the detector. The corresponding thermal time constant was 2.6 ms. The high values of responsivity and detectivity will allow for improved NETD to a value as low as 14 and 16 mK for an 8–9.4- and 9.4–10.8-μm window, respectively. These NETD values are higher than the current state of the art, for example, the Raytheon group's published results on VO_x microbolometers with a size of 25×25 μm^2 have achieved NETD less than 50 mk [38],

TABLE III
SUMMARY OF MODELING RESULTS AT 60 HZ. SUPPORT ARMS ARE DESIGNED
WITH LENGTHS OF 54 AND 25 μM. PERFORMANCE WAS ALSO CALCULATED
FOR TWO DIFFERENT ELECTRODE WIDTHS: 2 AND 4 μM. IN ALL CASES,
DEFLECTION OF THE MICROBOLOMETER PIXEL WAS MINIMAL

Parameter	Design 1	Design 2	Design 3	Design 4
Support arm dimensions	54×4 μm^2	54×2 μm^2	25×4 μm^2	25×2 μm^2
Responsivity (V/W)	1.23×10^5	1.66×10^5	7.512×10^4	1.303×10^5
Detectivity (cm Hz$^{1/2}$)/W	1.62×10^9	2.27×10^9	1.103×10^9	1.563×10^9
NETD 8–9.4 μm (mK)	14	10	21	15
NETD 9.4–10.8 μm (mK)	16	11	23	16
Total noise (V)	1.9×10^{-7}	1.827×10^{-7}	1.703×10^{-7}	2.083×10^{-7}
Thermal time constant (ms)	2.6	4.86	0.99	1.91
Thermal mass (J/K)	4.48×10^{-10}	4.16×10^{-10}	3.672×10^{-10}	3.525×10^{-10}
Thermal cond. (W/K)	1.71×10^{-7}	8.56×10^{-8}	3.696×10^{-7}	1.848×10^{-7}
Avg. absorption 8–9.4 μm (%)	61	61	61	61
Avg. absorption 9.4–10.8 μm (%)	63	63	63	63
Fill factor (%)	51	57	76	80

[39]. We expect the calculated NETD value will be higher if the readout electronic and system noise is included. The NETD is plotted versus chopper frequency in Fig. 8. The microbolometer performance was also calculated for narrower electrode arms and for shorter support arms. A complete list of the microbolometer performance results is shown in Table III. We have chosen the support arm dimensions as 54×4 μm^2 in all of the simulation results reported here because it represents an optimized value.

We also performed the simulation for three more designs. In all of these dimensions, the deflection of the microbolometer pixel was minimal. It is important to note that the performance of the microbolometer with shorter and narrower arms (25×2 μm^2) was similar to that achieved with a support arm size of 54×4 μm^2 and better fill factor. However, we selected the longer and wider arm because it can be fabricated with our current microfabrication capability.

VI. CONCLUSION

A dual-band microbolometer is designed based on semiconducting VO_X IR-sensitive material. The microbolometer's bottom mirror is switched between two metals to create two resonant vacuum cavities between the mirror and the suspended VO_X IR-sensitive material. The cavity depths maximize optical absorption in the 8–9.4- and 9.4–10.8-μm bands. The maximum optical absorption values observed were 65% and 59% for cavity depth of 3.9 and 4.63 μm, respectively. The achieved voltage responsivity was 1.23×10^5 V/W and the detectivity

was 1.62×10^9 cm sqrt(Hz)/W. In addition, the microbolometer NETD was between 14–16 mK. The calculated thermal time constant was 2.6 ms for each spectral band. Hence, these detectors could be used for 60-Hz frame rate applications.

REFERENCES

[1] R. Breiter, W. A. Cabanski, K.-H. Mauk, W. Rode, J. Ziegler, H. Schneider, and M. Walther, "Multicolor and dual-band IR camera for missile warning and automatic target recognition," in *Proc. SPIE—Int. Soc. Opt. Eng.*, 2002, vol. 4718, pp. 280–288.
[2] P. Ljungberg, R. G. Kihlen, S. H. Lundqvist, P. Potet, and S. Berrebi, "Multispectral imaging MWIR sensor for determination of spectral target signatures," in *Proc. SPIE—Int. Soc. Opt. Eng.*, 1997, vol. 3061, pp. 823–832.
[3] L. Becker, "Multicolor LWIR focal plane array technology for space- and ground-based applications," in *Proc. SPIE—Int. Soc. Opt. Eng.*, 2004, vol. 5564, pp. 1–14.
[4] L. Becker, "Novel quantum well, quantum dot, and superlattice heterostructure based infrared detectors," in *Proc. SPIE—Int. Soc. Opt. Eng.*, 2009, vol. 7298, p. 729805.
[5] M. Nagashima, M. Kibe, Mi. Doshida, H. Yamashita, R. Suzuki, Y. Uchiyama, Y. Matsukura, H. Nishino, T. Fujii, and S. Miyazaki, "High-performance 256 × 256 pixel LWIR QDIP," in *Proc. SPIE—Int. Soc. Opt. Eng.*, 2009, vol. 7298, p. 72980D.
[6] P. Bensussan, P. Tribolet, G. Destéfanis, and M. Sirieix, "Fifty years of successful MCT research and production in France," in *Proc. SPIE—Int. Soc. Opt. Eng.*, 2009, vol. 7298, p. 72982N.
[7] A. Dutta, R. Sengupta, A. Krishnan, S. Islam, P. S. Wijewarnasuriya, and N. Dhar, "Broadband image sensors for biomedical, security, and automotive applications," in *Proc. SPIE—Int. Soc. Opt. Eng.*, 2007, vol. 6769, p. 67690C.
[8] D. K. Breakfield and D. Plemons, "The application of microbolometers in 360° ground vehicle situational awareness," in *Proc. SPIE—Int. Soc. Opt. Eng.*, 2009, vol. 7298, p. 72981K.
[9] R. Breiter, J. Wendler, H. Lutz, S. Rutzinger, K. Hofmann, and J. Ziegler, "IR-detection modules from SWIR to VLWIR: Performance and applications," in *Proc. SPIE—Int. Soc. Opt. Eng.*, 2009, vol. 7298, p. 72981W.
[10] M. Münzberg, R. Breiter, W. Cabanski, K. Hofmann, H. Lutz, J. Wendler, J. Ziegler, R. Rehm, and M. Walther, "Dual color IR detection modules, trends and applications," in *Proc. SPIE—Int. Soc. Opt. Eng.*, 2007, vol. 6542, p. 654207.
[11] W.-B. Song and J. J. Talghader, "Design and characterization of adaptive microbolometers," *J. Micromech. Microeng.*, vol. 16, pp. 1073–1079, 2006.
[12] A. K. Sood, Y. R. Puri, R. Richwine, L. Becker, N. Dhar, S. Sivanathan, and J. Zimmerman, "Advances in multi-color large area focal plane array sensors for standoff detection," in *Proc. SPIE—Int. Soc. Opt. Eng.*, 2005, vol. 5881, p. 58810N.
[13] P. W. Norton, S. Cox, B. Murphy, K. Grealish, M. Joswick, B. Denley, F. Feda, L. Elmali, and M. Kohin, "Uncooled thermal imaging sensor and application advances," in *Proc. SPIE—Int. Soc. Opt. Eng.*, 2006, vol. 6206, p. 620617.
[14] D. Murphy, M. Ray, A. Kennedy, J. Wyles, C. Hewitt, R. Wyles, E. Gordon, T. Sessler, S. Baur, D. Van Lue, S. Anderson, R. Chin, H. Gonzalez, C. Le Pere, S. Ton, and T. Kostrzewa, "Expanded applications for high performance VO$_x$ microbolometer FPAs," in *Proc. SPIE—Int. Soc. Opt. Eng.*, 2005, vol. 5783, p. 448.
[15] D. Murphy, M. Ray, A. Kennedy, J. Wyles, C. Hewitt, R. Wyles, E. Gordon, T. Sessler, S. Baur, D. Van Lue, S. Anderson, R. Chin, H. Gonzalez, C. Le Pere, S. Ton, and T. Kostrzewa, "Two-color HgCdTe infrared staring focal plane arrays," in *Proc. SPIE*, 2003, vol. 5209, pp. 1–13.
[16] L. S. R. Becker, "Multicolor LWIR focal plane array technology for space- and ground-based applications," in *Proc. SPIE—Int. Soc. Opt. Eng.*, 2004, vol. 5564, p. 1.
[17] A. C. Goldberg, "Application of dual-band infrared focal plane arrays to tactical and strategic military problems," in *Proc. SPIE—Int. Soc. Opt. Eng.*, 2003, pp. 500–514.
[18] S. Han, J. Jung, and D. P. Neikirk, "Wavelength selective bolometer design," *Int. J. High Speed Electron. Syst.*, vol. 18, no. 3, pp. 569–574, 2008.
[19] V. N. Leonov and D. P. Butler, "Two-color thermal detector with thermal chopping for infrared focal-plane arrays," *Appl. Opt.*, vol. 40, no. 16, pp. 2601–2610, 2001.

[20] Y. Wang, B. J. Potter, and J. J. Talghader, "Coupled absorption filters for thermal detectors," *Opt. Lett.*, vol. 31, no. 13, pp. 1945–1947, 2006.

[21] S. Paradis, P. Merel, P. Laou, and D. Alain, "Vanadium oxide films for optical modulation applications," in *Proc. SPIE—Int. Soc. Opt. Eng.*, 2006, vol. 6343, p. 63433U.

[22] S. Paradis, "Tailoring electro-optical properties of RF sputtered vanadium dioxide with dopant for smart infrared modulation," in *Proc. Int. Workshop Smart Mater. Structures*, Oct. 23–24, 2008, pp. 281–290.

[23] G. Golan, A. Axelevitch, B. Sigalov, and B. Gorenstein, "Investigation of phase transition mechanism in vanadium oxide thin films," *J. Optoelectron. Adv. Mater.*, vol. 6, no. 1, pp. 189–195, 2004.

[24] P. P. Boriskov, A. L. Pergament, A. A. Velinchko, G. B. Stefanovich, and N. A. Kuldin, Metal-Insulator Transition in Electric Field: A Viewpoint From the Switching Effect 2006, reprint arXiv:cond-mat/0603132.

[25] L. A. Luz de Almeida, G. S. Deep, A. M. N. Lima, and H. Neff, "Modeling of the hysteretic metal-insulator transition in a vanadium dioxide infrared detector," *Opt. Eng.*, vol. 41, no. 10, pp. 2582–2588, 2002.

[26] X. Chena and J. Daib, "Optical switch with low-phase transition temperature based on thin nanocrystalline VO_x film," Optik, Advance Copy 2009.

[27] M. Soltani and M. Chaker, "1×2 optical switch devices based on semiconductor-to-metallic phase transition characteristics of VO_2 smart coatings," *Meas. Sci. Technol.*, vol. 17, pp. 1052–1056, 2006.

[28] T. Schimert, C. Hanson, J. Brady, T. Fagan, M. Taylor, W. McCardel, R. Gooch, M. Gohlke, and A. J. Syllaios, "Advances in small-pixel, large-format—Si bolometer arrays," in *Proc. SPIE—Int. Soc. Opt. Eng.*, 2009, vol. 7298, p. 72980T.

[29] M. Almasri, D. P. Butler, and Z. Çelik-Butler, "Self-supporting semiconducting Y-Ba-Cu-O uncooled IR microbolometers with low-thermal mass," *J. Microelectromech. Syst.*, vol. 10, no. 3, pp. 469–476, Sep. 2001.

[30] A. H. Z. Ahmed, R. N. Tait, T. B. Oogarah, H. C. Liu, M. W. Denhoff, G. I. Sproule, and M. J. Graham, "A surface micromachined amorphous $Ge_xSi_{1-x}O_y$ bolometer for thermal imaging applications," *Proc. SPIE—Int. Soc. Opt. Eng.*, vol. 5578, pp. 298–308, 2004.

[31] Q. Cheng and M. Almasri, "Silicon germanium oxide ($Si_xGe_{1-x}O_y$) infrared material for uncooled infrared detection," in *Proc. SPIE—Int. Soc. Opt. Eng.*, 2009, vol. 7298, p. 72980K.

[32] M. M. Rana and D. P. Butler, "Radio frequency sputtered $Si_{1-x}Ge_x$ and $Si_{1-x}Ge_xO_y$ thin films for uncooled infrared detectors," *Thin Solid Films*, vol. 514, pp. 355–360, 2006.

[33] M. V. S. Ramakrishna, G. Karunasiri, U. Sridhar, and G. Chen, "Performance of titanium and amorphous germanium microbolometer infrared detectors," in *Proc. SPIE—Int. Soc. Opt. Eng.*, 1999, vol. 3666, pp. 415–420.

[34] P. W. Kruse and D. D. Skatrud, "Uncooled infrared imaging arrays and systems," in *Semiconductors and Semimetals*. New York: Academic, 1997, vol. 47, pp. 17–42.

[35] P. W. Kruse, "The design of uncooled infrared imaging arrays," in *Proc. SPIE—Int. Soc. Opt. Eng.*.

[36] S. J. Ropson, J. F. Brady, III, G. L. Francisco, J. Gilstrap, R. W. Gooch, P. McCardel, B. Ritchey, and T. R. Schimert, "A-Si 160×120 Micro IR camera: Operational performance," in *Proc. SPIE—Int. Soc. Opt. Eng.*, 2001, vol. 4393, pp. 89–98.

[37] F. Guinneton, L. Sauques, J.-C. Valmalette, F. Cros, and J.-R. Gavarri, "Optimized infrared switching properties in thermochromic vanadium dioxide thin films: Role of deposition process and microstructure," *Thin Solid Films*, vol. 446, pp. 287–295, 2004.

[38] S. Black, M. Ray, C. Hewitt, R. Wyles, E. Gordon, K. Almada, S. Baur, M. Kuiken, D. Chi, and T. Sessler, "RVS uncooled sensor development for tactical applications," in *Proc. SPIE—Int. Soc. Opt. Eng.*, 2008, vol. 6940, p. 694022.

[39] D. Murphy *et al.*, "640×512 17 μm Microbolometer FPA and sensor development," in *Proc. SPIE—Int. Soc. Opt. Eng.*, 2007, vol. 6542, p. 65421Z.

Qi Cheng (S'09) received the B.Sc. and M.Sc. degrees from Nanjing University of Science and Technology, Nanjing, China, in 2000 and 2003, respectively, and the M.Sc. degree from the Royal Institute of Technology (KTH), Sweden in 2006, all in electrical engineering. He is currently working toward the Ph.D. degree in electrical engineering at the University of Missouri, Columbia.

His current research interests include MEMS and bioMEMS design and fabrication, characterization of infrared sensing material silicon germanium oxide thin film (SiGeO), optical, thermal, and mechanical design and modeling of uncooled tunable microbolometers for infrared detection, and micropost array bio-sensor for cardiovascular cell traction force studies.

Suzanne Paradis received the B.Eng. degree in engineering physics from Université Laval, Quebec, QC, Canada in 1991, and the M.Sc. degree in materials engineering from the New Mexico Institute of Mining and Technology, Socorro, in 1995.

She was a Senior Materials Analyst with IBM Canada, Bromont, from 1991 to June 2004. Her expertise includes microelectronic packaging analysis and materials characterization techniques such as scanning electron microscopy and X-ray diffraction. She joined the Micro Systems Group, Defence Research and Development Canada, Valcartier, ON, Canada, in 2004, where her research interests include smart thin-film materials for applications in electrooptic devices, microfabrication and electrooptic characterization.

Truc Bui is currently working toward the B.S. degree at the University of Missouri, Columbia.

Her current research interests include silicon germanium oxide infrared (IR) materials for uncooled IR detection, modeling, and simulation of uncooled IR detectors, microfabrication, and MEMS.

Ms. Truc is a member of the Tau Beta Pi and Eta Kappa Nu. She was the recipient of the College of Engineering Scholarship over the last three years and was awarded the 2009 Junior Outstanding Award in Electrical Engineering.

Mahmoud Almasri (M'09) received the B.Sc. and M.Sc. degrees in physics from Bogazici University, Istanbul, Turkey, in 1995 and 1997, respectively, and the Ph.D. degree in electrical engineering from Southern Methodist University (SMU), Dallas, TX, in 2001.

He is currently an Assistant Professor with the Department of Electrical and Computer Engineering, University of Missouri, Columbia. From 2001 to 2002, he was a Research Scientist with General Monitors, Lake Forest, CA. From 2002 to 2003, he was with Albanynanotech, Albany, NY, as a Postdoctoral Research Associate, and, from 2004 to 2005, he was with the Georgia Institute of Technology as a Postdoctoral Fellow, and then promoted to a Research Scientist. His current research interests include 3-D biosensors, MEMS capacitor for power harvesting, IR materials (Si-Ge-O) and detectors, MEMS-based Coulter counter for cell sizing, micropost arrays for measuring cell traction forces, and 3-D microscaffolds for brain slice studies in vitro. His research is currently funded by the National Science Foundation, ARO, USDA, the Leonard Wood Institute, the Department of Energy, and DND Canada.